COMPUTATION OF LEADING-EDGE VORTEX FLOWS

Richard W. Newsome
Air Force Wright Aeronautical Laboratories
AFSC Liaison Office, NASA Langley Research Center
Hampton, Virginia

James L. Thomas
NASA Langley Research Center
Hampton, Virginia

SUMMARY

The simulation of the leading-edge vortex flow about a series of conical delta wings through solution of the Navier-Stokes and Euler equations is studied. The occurrence, the validity, and the usefulness of separated flow solutions to the Euler equations are of particular interest. Central and upwind difference solutions to the governing equations are compared for a series of cross-sectional shapes, including both rounded and sharp tip geometries.

For the rounded leading edge and the flight condition considered, viscous solutions obtained with either central or upwind difference methods predict the classic structure of vortical flow over a highly swept delta wing. Predicted features include the primary vortex due to leading-edge separation and the secondary vortex due to crossflow separation. Central difference solutions to the Euler equations show a marked sensitivity to grid refinement. On a coarse grid, the flow separates due to numerical error and a primary vortex which resembles that of the viscous solution is predicted. In contrast, the upwind difference solutions to the Euler equations predict attached flow even for first-order solutions on coarse grids. On a sufficiently fine grid, both methods agree closely and correctly predict a shock-curvature-induced inviscid separation near the leeward plane of symmetry.

Upwind difference solutions to the Navier-Stokes and Euler equations are presented for two sharp leading-edge geometries. The viscous solutions are quite similar to the rounded leading-edge results with vortices of similar shape and size. The upwind Euler solutions predict attached flow with no separation for both geometries. However, with sufficient grid refinement near the tip or through the use of more accurate spatial differencing, leading-edge separation results. Once the leading-edge separation is established, the upwind solution agrees with recently published central difference solutions to the Euler equations.

INTRODUCTION

The current interest in high angle-of-attack aerodynamics and vortical flows has focused considerable attention on the numerical simulation of the flow about a swept delta wing at moderate to high angles of attack. For subsonic leading edges which are sharp or of small radius of curvature, the flow separates at the tips and forms two counter-rotating vortices on opposite sides of the leeward wing surface. The presence of the vortices produces a pressure minimum on the upper surface and results in an additional lift component not predicted by linear theory.

Interest, here, is restricted to methods which "capture" the vortex rather than modeling it in an approximate manner. Thus, we consider only methods which solve the Euler and Navier-Stokes equations. The Navier-Stokes equations model all physical mechanisms and provide the most accurate results. Vigneron et al.[1] solved the conical and parabolic approximations to the Navier-Stokes equations for the vortical flow about a sharp-edged delta wing at supersonic speeds. Fujii and Kutler[2,3] solved the three-dimensional Navier-Stokes equations for the leading-edge separation about a delta wing with rounded edges at subsonic speeds. Rizzetta and Shang[4] presented three-dimensional Navier-Stokes solutions for a delta wing with sharp edges at supersonic and hypersonic speeds. The principal drawbacks of the Navier-Stokes equations are the higher computational costs necessary to resolve small-scale viscous effects and the need to model turbulence in an approximate manner. However, the Navier-Stokes solutions set the standard by which less exact solutions must be judged.

In the last several years, it has been suggested that Euler codes could be the method of choice in the simulation of leading-edge vortex flows.[5] In contrast to potential methods, the Euler equations provide the correct Rankine-Hugoniot shock jump conditions. They also admit rotational flow solutions. Indeed, numerous Euler solutions with leading-edge separation have been reported for both rounded and sharp leading edges using a variety of numerical schemes. A partial list includes the works of Rizzi et al.[6-10], Raj and Sikora,[11] and Powell, Murman et al.[12] using a finite volume Runge-Kutta algorithm; Fujii and Obayashi[13] using a LU factored scheme whose right-hand side is identical to the Beam and Warming scheme; and Manie et al.[14] and Newsome[15] using a MacCormack scheme.

Since flow separation is usually associated with generation of vorticity through the no-slip boundary condition in a viscous flow, its occurrence in an inviscid solution is of both theoretical and practical importance. Necessary conditions for flow separation include the presence of vorticity in the flow as well as an adverse pressure gradient. While the Euler equations admit rotational solutions through the transport (and for three-dimensional flow, stretching) of vorticity, there is only one valid mechanism for vorticity generation in an inviscid flow. In accord with Crocco's theorem, the Euler equations allow for the generation of vorticity through non-constant shock strength (shock curvature, shock intersection, etc.). Salas[16] first demonstrated shock-induced inviscid separation for the transonic flow about a circular cylinder. Marconi[17] published similar results for the supersonic flow about circular cones and more recently elliptic cones.[18]

The Euler equations are singular at a sharp tip. This, however, causes no particular problem for a finite volume scheme in which cell centered quantities are computed. Salas and Daywitt[19], in considering conical flow about sharp external axial corners, have shown that a limiting form of the inviscid equations valid at the singular corner point leads to a conical analog of the isentropic Prandtl-Meyer expansion. The maximum Prandtl-Meyer expansion angle corresponds to vacuum pressure. It is not clear whether theoretically valid attached flow Euler solutions exist for geometries in which the vacuum expansion limit is exceeded. For any finite radius of curvature, the flow field is resolvable and a valid Euler solution must approach the expansion limit as the radius of curvature approaches zero. In a viscous gas, the flow separates well before the inviscid expansion limit is reached. Once the

separation and the level of shed vorticity are established, the dynamics of the vortex motion, i.e. its interaction with neighboring surfaces, are essentially inviscid and thus adequately described by the Euler equations (excluding viscous features such as secondary vortices).

In practice, numerical solutions to the Euler equations for wings of small radius of curvature often result in inviscid separation. Any numerical algorithm, whether central or upwind differenced, must be dissipative for stability. As such, there is an effective Reynolds number inherent in the calculation which is dependent on the local mesh resolution and the order of the method. Upwind schemes are naturally dissipative. Central difference schemes are not naturally dissipative and dissipative terms are generally added to the discretized equations. The added dissipative terms are generally of two types: a third-order fourth-difference term to provide dissipation in smooth regions and an adaptive second difference term to control shock oscillations. The latter term reverts to first order at a shock but it also is significant in regions of rapid expansion. Finally, error can be introduced by the application of surface boundary conditions.

In reference 15, from which parts of this paper are taken, central difference solutions to the Euler and Navier-Stokes equations for the flow about a delta wing with a rounded leading edge (elliptic cone) were considered. The separation vortex predicted with the Euler equations, which is characteristic of the viscous solution, was found to be numerically induced. More recently, upwind difference Euler solutions[20] were shown to be much less susceptible to spurious inviscid separation. In the present paper, the upwind difference method is extended to the conical Navier-Stokes equations and a more detailed comparison of central and upwind difference solutions for both the Euler and Navier-Stokes equations is given for the round leading-edge wing. The upwind code is further extended to consider Navier-Stokes and Euler solutions for several sharp leading-edge wings.

SOLUTION METHOD

If interest is restricted to supersonic flow past conical bodies, then the governing equations may be simplified since the resulting flow will also be conical. A conical flow has the property that all flow quantities are invariant on rays which pass through the apex of the conical surface. All derivatives in the radial direction may then be neglected, reducing a three-dimensional problem into a much more tractable two-dimensional one. The conical assumption is exact for inviscid flow. For viscous flow, a length scale dependence is contained in the Reynolds number. The flow may be thought of as locally conical with the Reynolds number determining the location of the conical plane at which the solution is determined. The conical equations may be obtained by introduction of the conical variables

$$\xi = \xi(x) = x \qquad Y = \frac{y}{x} \qquad Z = \frac{z}{x}$$

$$\eta = \eta(x,y,z) = \eta(Y,Z)$$

$$\zeta = \zeta(x,y,z) = \zeta(Y,Z)$$

into the three-dimensional Navier-Stokes equations, written in terms of the non-dimensional Cartesian variables (x,y,z). Upon simplifying for conical flow, the govering equations may be expressed in conservation form as

$$\frac{\partial}{\partial t}(\hat{Q}) + \frac{\partial}{\partial \eta}(\hat{G} - \hat{G}_v) + \frac{\partial}{\partial \zeta}(\hat{H} - \hat{H}_v) + (\hat{S} - \hat{S}_v) = 0 \qquad (1)$$

The inviscid equations are obtained by dropping the terms $(\hat{G}_v, \hat{H}_v, \hat{S}_v)$.

The general three-dimensional, upwind, Euler/thin layer Navier-Stokes code developed by Thomas[20,21] was specialized for conical flow. In the finite volume formulation, a single array of crossflow plane volumes was constructed such that the inflow and outflow surfaces are scaled by the conical transformation, as above. While the code uses a finite volume approach, the equations may be written in generalized coordinates as

$$\frac{\partial}{\partial t}(\hat{Q}) + \frac{\partial}{\partial \xi}(\hat{F}) + \frac{\partial}{\partial \eta}(\hat{G}) + \frac{\partial}{\partial \zeta}(\hat{H} - \hat{H}_v) = 0 \qquad (2)$$

At each iteration, the inflow conditions are updated with the results of the previous iteration so that, at convergence, $\partial\hat{Q}/\partial\xi = 0$, consistent with the conical flow approximation.

The inviscid and viscous flux vectors in equations (1) and (2) are defined as

$$\hat{Q} = \frac{Q}{J} = \frac{1}{J}\begin{bmatrix} \rho \\ \rho u \\ \rho v \\ \rho w \\ \rho E \end{bmatrix} \qquad \hat{F},\hat{G},\hat{H} = \frac{1}{J}\begin{bmatrix} \rho U_c \\ \rho U_c u + \alpha_x p \\ \rho U_c v + \alpha_y p \\ \rho U_c w + \alpha_z p \\ [\rho E + p]U_c \end{bmatrix} \qquad (3)$$

$$\hat{S} = \frac{2}{J}\begin{bmatrix} \rho u \\ \rho u^2 + p \\ \rho uv \\ \rho uw \\ [\rho E + p]u \end{bmatrix}$$

$$E = e_I + \frac{1}{2}(u^2 + v^2 + w^2)$$

$$U_c = \alpha_x u + \alpha_y v + \alpha_z w$$

$$\hat{G}_v, \hat{H}_v = \frac{1}{J}\begin{bmatrix} 0 \\ \alpha_x \tau_{xx} + \alpha_y \tau_{xy} + \alpha_z \tau_{xz} \\ \alpha_x \tau_{xy} + \alpha_y \tau_{yy} + \alpha_z \tau_{yz} \\ \alpha_x \tau_{xz} + \alpha_y \tau_{yz} + \alpha_z \tau_{zz} \\ \alpha_x b_x + \alpha_y b_y + \alpha_z b_z \end{bmatrix} \qquad \hat{S}_v = \frac{1}{J}\begin{bmatrix} 0 \\ \tau_{xx} \\ \tau_{xy} \\ \tau_{xz} \\ b_x \end{bmatrix}$$

Although the flux vectors can be written in a common form, they are in fact quite different as applied to equations (1) or (2). A general three-dimensional transformation between the Cartesian variables (x,y,z) and the computational variables is implied in equation (2), so that the flux terms can be defined as below:

$$\begin{aligned} \hat{F}: &\quad \alpha = \xi;\ U_c = U = \xi_x u + \xi_y v + \xi_z w \\ \hat{G}: &\quad \alpha = \eta;\ U_c = V = \eta_x u + \eta_y v + \eta_z w \\ \hat{H}, \hat{H}_v: &\quad \alpha = \zeta;\ U_c = W = \zeta_x u + \zeta_y v + \zeta_z w \\ J &= \partial(\xi,\eta,\zeta)/\partial(x,y,z) \end{aligned} \tag{4}$$

In the finite volume formulation, expressions for the transformation derivatives and the Jacobain, J, are evaluated geometrically.

When working with the conical equations (1), it is convenient to work in terms of the conical variables, Y and Z. This allows a simpler form for the equations using the two-dimensional transformation:

$$\begin{bmatrix} \eta_Y & \zeta_Y \\ \eta_Z & \zeta_Z \end{bmatrix} = \begin{bmatrix} Y_\eta & Z_\eta \\ Y_\zeta & Z_\zeta \end{bmatrix}^{-1} \qquad J = \begin{vmatrix} \eta_Y & \zeta_Y \\ \eta_Z & \zeta_Z \end{vmatrix}$$

Since

$$\begin{aligned} \eta_x &= -\frac{1}{x}\left[Y\eta_Y + Z\eta_Z\right] \qquad \zeta_x = -\frac{1}{x}\left[Y\zeta_Y + Z\zeta_Z\right] \\ \eta_y &= \frac{1}{x}\left[\eta_Y\right] \qquad \zeta_y = \frac{1}{x}\left[\zeta_Y\right] \\ \eta_z &= \frac{1}{x}\left[\eta_Z\right] \qquad \zeta_z = \frac{1}{x}\left[\zeta_Z\right] \end{aligned} \tag{5}$$

it is convenient to define the terms

$$\eta_X = -\left[Y\eta_Y + Z\eta_Z\right] \qquad \zeta_X = -\left[Y\zeta_Y + Z\zeta_Z\right]$$

so that the flux terms in equation (3) can be defined as

$$\hat{G},\hat{G}_v: \quad \alpha = \eta;\ (\alpha_x,\alpha_y,\alpha_z) = (\eta_X,\eta_Y,\eta_Z) \qquad U_c = V = \eta_X u + \eta_Y v + \eta_Z w$$

$$\hat{H},\hat{H}_v: \quad \alpha = \zeta;\ (\alpha_x,\alpha_y,\alpha_z) = (\zeta_X,\zeta_Y,\zeta_Z) \qquad U_c = W = \zeta_X u + \zeta_Y v + \zeta_Z w \tag{6}$$

The term, $\frac{1}{x}$, is absorbed into equation (1) when the Reynolds number and the time scale are defined with respect to the length scale, L, where L is the length from the body apex to the crossflow solution plane.

Upon nondimensionalization in terms of the freestream density, ρ_∞ and sound speed, c_∞, the shear stress and heat flux terms are defined in tensor notation (summation convention implied) as:

$$\tau_{x_\alpha x_\beta} = \frac{1}{Re_\infty}\left[\mu\left(\frac{\partial u_\alpha}{\partial x_\beta} + \frac{\partial u_\beta}{\partial x_\alpha}\right) + \lambda\frac{\partial u_\gamma}{\partial x_\gamma}\,\delta_{\alpha\beta}\right]$$

$$\dot{q}_{x_\alpha} = -\left(\frac{M_\infty}{Re_\infty Pr(\gamma-1)}\right)\frac{\partial c^2}{\partial x_\alpha} \qquad b_{x_\alpha} = u_\beta \tau_{x_\alpha x_\beta} - \dot{q}_{x_\alpha} \tag{7}$$

$$Re_\infty = \frac{\rho_\infty u_\infty L}{\mu_\infty}$$

The chain rule is used to evaluate derivatives with respect to (x,y,z) in terms of (η,ζ). When the thin layer assumption is made, only those derivatives in the direction normal to the wall (ζ) are retained in the stress and heat flux terms. Equations (1) and (2) are closed by the perfect gas equation of state and Sutherland's law for molecular viscosity. All calculations are for laminar flow only.

The conical flow equations (1) were solved with the MacCormack[22] unsplit, explicit finite-difference algorithm. Since the algorithm is well known, a detailed description is unnecessary. The method is second-order accurate in space and time and is conditionally stable. To control shock oscillations, MacCormack's[23] pressure damping was incorporated into the scheme. The damping term is $0(\Delta x^3)$ except in regions of large pressure gradients where the pressure gradient switch forces the damping to $0(\Delta x)$. MacCormack's scheme is also naturally dissipative due to unsymmetric differencing in the predictor and corrector steps.

Upwind solutions were obtained with the flux vector splitting algorithm developed by Thomas.[20] The generalized fluxes $\hat{F},\hat{G},\hat{H}$, representing pressure and convection terms are split into forward and backward contributions according to the sign of the eigenvalues of the Jacobian matrices

$\partial\hat{F}/\partial Q,\ \partial\hat{G}/\partial Q,\ \partial\hat{H}/\partial Q$

and differenced accordingly. For example, the flux difference in the ξ-direction is

$$\delta_\xi \hat{F} = \delta_\xi^- \hat{F}^+ + \delta_\xi^+ \hat{F}^- \tag{8}$$

where δ_ξ^- and δ_ξ^+ denote general backward and forward divided difference operators respectively, in the ξ-direction. In reference 20, van Leer's flux vector splitting was extended to three-dimensional generalized coordinates. The flux, $\hat{F}$, as an example, is split according to the contravariant Mach number in the ξ-direction, defined as $M_\xi = \bar{u}/c$, where $\bar{u} = U/\left|\text{grad}(\xi)\right|$. For supersonic flow, $\left|M_\xi\right| \geq 1$

$$\begin{aligned} \hat{F}^+ &= \hat{F},\ \hat{F}^- = 0 \quad M_\xi \geq +1 \\ \hat{F}^- &= \hat{F},\ \hat{F}^+ = 0 \quad M_\xi \leq -1 \end{aligned} \tag{9}$$

and for subsonic flow, $\left|M_\xi\right| < 1$

$$\hat{F}^\pm = \frac{\left|\text{grad}\xi\right|}{J} \begin{bmatrix} f^\pm_{mass} \\ f^\pm_{mass}\left[\hat{k}_x(-\bar{u} \pm 2c)/\gamma + u\right] \\ f^\pm_{mass}\left[\hat{k}_y(-\bar{u} \pm 2c)/\gamma + v\right] \\ f^\pm_{mass}\left[\hat{k}_z(-\bar{u} \pm 2c)/\gamma + w\right] \\ f^\pm_{energy} \end{bmatrix} \tag{10}$$

where

$$f^\pm_{mass} = \pm\rho c(M_\xi \pm 1)^2/4$$

$$f^\pm_{energy} = f^\pm_{mass}\left[\left\{-(\gamma-1)\bar{u}^2 \pm 2(\gamma-1)\bar{u}c + 2c^2\right\}/(\gamma^2-1) + \frac{1}{2}(u^2+v^2+w^2)\right]$$

The surface area of the cell interface in the ξ direction is $\left|\text{grad}\xi\right|/J$, the cell volume is $1/J$, and

$$(\hat{k}_x, \hat{k}_y, \hat{k}_z) = (\xi_x, \xi_y, \xi_z)/\left|\text{grad}\xi\right| \tag{11}$$

are the direction cosines of the cell interfaces in the ξ direction. The split-flux differences are implemented as a flux balance across a cell as (for $\Delta\xi = \Delta\eta = \Delta\zeta = 1$)

$$\delta_\xi^- \hat{F}_i^+ + \delta_\xi^+ \hat{F}_i^- = \left[\hat{F}^+(Q^-) + \hat{F}^-(Q^+)\right]_{i+1/2} - \left[\hat{F}^+(Q^-) + \hat{F}^-(Q^+)\right]_{i-1/2} \tag{12}$$

The notation $\hat{F}^+(Q^-)_{i+1/2}$ denotes a forward flux evaluated using the metric terms at the cell interface (i+1/2), with conserved variables obtained by an upwind biased interpolation

$$Q^-_{i+1/2} = Q_i + \frac{1}{4}\phi_\xi\left[(1-\kappa_\xi)\nabla_\xi + (1+\kappa_\xi)\Delta_\xi\right]Q_i$$

$$Q^+_{i+1/2} = Q_{i+1} - \frac{1}{4}\phi_\xi\left[(1+\kappa_\xi)\nabla_\xi + (1-\kappa_\xi)\Delta_\xi\right]Q_{i+1} \tag{13}$$

where

$$\Delta_\xi Q_i = Q_{i+1} - Q_i \qquad \nabla_\xi Q_i = Q_i - Q_{i-1}$$

Only fully upwind first or second-order accurate differencing has been used in the results that follow:

$$\phi_\xi = 0 \qquad \text{(first-order upwind)}$$
$$\phi_\xi = 1,\ \kappa_\xi = -1 \qquad \text{(second-order upwind)} \tag{14}$$

Differencing for the diffusion terms representing shear stress and heat transfer effects corresponds to second-order central differences in which second derivatives are treated as differences across cell interfaces of first derivative terms

$$\delta_\zeta \hat{H}_{v_k} = \hat{H}_{v_{k+1/2}} - \hat{H}_{v_{k-1/2}} \tag{15}$$

where, for example, the term,

$$\tau_{xy} = \frac{M_\infty}{Re_\infty}\left[\mu\left(\frac{\partial u}{\partial y} + \frac{\partial v}{\partial x}\right)\right]$$

under the thin layer approximation, becomes,

$$\tau_{xy} = \left(\frac{M_\infty}{Re_\infty}\right)\mu\left(\zeta_y\frac{\partial u}{\partial \zeta} + \zeta_x\frac{\partial v}{\partial \zeta}\right) \tag{16}$$

and is differenced in $\hat{H}_{v_{k\pm1/2}}$ as

$$\frac{M_\infty}{Re_\infty}\mu_{k\pm1/2}\left(\zeta_{y_{k\pm1/2}}\delta_\zeta u_{k\pm1/2}+\zeta_{x_{k\pm1/2}}\delta_\zeta v_{k\pm1/2}\right) \tag{17}$$

where

$$\delta_\zeta u_{k+1/2} = u_{k+1} - u_k$$

The linearized, backward time approximation in delta form for the three-dimensional equations is given as

$$\left[\frac{I}{J\Delta t}+\delta_\xi\frac{\partial\hat{F}}{\partial Q}+\delta_\eta\frac{\partial\hat{G}}{\partial Q}+\delta_\zeta\left(\frac{\partial\hat{H}}{\partial Q}-\frac{\partial\hat{H}_v}{\partial Q}\right)\right]\Delta Q = R^N \tag{18}$$

As described in reference 20, equation (18) is solved by streamwise relaxation (ξ-direction) and approximate factorization in the crossflow plane as

$$\left[M+\delta_\eta\frac{\partial\hat{G}}{\partial Q}\right][M]^{-1}\left[M+\delta_\zeta\left(\frac{\partial\hat{H}}{\partial Q}-\frac{\partial\hat{H}_v}{\partial Q}\right)\right]\Delta Q = R(Q^N, Q^{N+1}) \tag{19}$$

where

$$M = \left[\frac{I}{J\Delta t}+\frac{\partial\hat{F}^+}{\partial Q}-\frac{\partial\hat{F}^-}{\partial Q}\right]$$

In general, the solution is obtained by alternate forward and backward sweeping through the crossflow planes with a nonlinear update of the residual R indicated on the right side of (19). For the degenerate conical flow case, this corresponds to reinitialization of the inflow plane and update of the crossflow plane until convergence is achieved. Since the spatial implicit discretizations may be taken as first order with no loss in steady-state accuracy, the solution of equation (19) involves the solution of two block tridiagonal equations.

Initial conditions for both central and upwind difference methods consisted of freestream conditions. Boundary conditions consisted of freestream conditions on the outer boundary, reflection conditions in the crossflow symmetry plane and slip or no slip conditions on the body surface depending upon whether the viscous or inviscid equations are considered.

RESULTS

The flow about several different conical delta wings with a 70° wing sweep angle at a Mach number of 2 and 10 degrees angle of attack was chosen for study. A thin elliptic cone, Fig. 1, with half angles, $\tan^{-1}(y_{LE}/x)$ =

20°, and $\tan^{-1}(z_{CL}/x) = 1.5°$, was used as a model for round leading edges with small curvature radius. For sharp tips, a thinner conical body was defined with a vertical half angle, $\tan^{-1}(z_{CL}/x) = 0.75°$ and a tip half angle angle given as $\tan^{-1}(dz/dy)_{LE} = 10°$. As an extreme case, a zero thickness flat delta wing was also considered.

Central and upwind difference solutions to the Navier-Stokes and Euler equations are compared for the rounded leading-edge wing. Upwind difference Euler and Navier-Stokes results are then presented for the sharp tip geometries.

ROUNDED LEADING EDGES

Navier-Stokes Solutions

A comparison of central and upwind difference calculations was made at Reynolds numbers of $Re_\infty = 0.1 \times 10^6$ and 0.5×10^6. The grid consisted of 151 points around and 65 points normal to the body with an equal minimum step size at the tip, in both directions, $\Delta s/x = .0002$. This minimum step size in the body normal direction was relaxed to a maximum value $\Delta s/x = .0006$ away from the tip. The grid and an enlarged view of the tip are shown in Fig. 2. At a Reynolds number of $Re_\infty = 0.1 \times 10^6$, the windward symmetry plane boundary layer contained 14 points and the leading-edge boundary layer contained 7 points.

In general, central and upwind difference solutions, both second-order accurate, are in good agreement. A plot of the crossflow velocity for the central difference solution is shown in Fig. 3 (the upwind result is nearly identical). In this and the results to follow, the radial velocity component has been subtracted out of the Cartesian crossflow components. The flow separates at the leading edge with a large primary vortex and a smaller secondary vortex. At the higher Reynolds number, $Re_\infty = 0.5 \times 10^6$, the secondary vortex is smaller relative to the primary vortex. A comparison of pressure coefficients, Fig. 4, for both the central and upwind difference solutions, shows the suction peak to be stronger for the higher Reynolds number. At the higher Reynolds number, minor differences appear in the two solutions in the separation zone, particularly near the leading edge.

Squire[24] presented experimental data for the same elliptic cone with a small circular centerbody. To verify the viscous calculations, the upwind scheme was applied to the elliptic cone at conditions corresponding to the experimental data of Squire: $M_\infty = 1.8$, $Re_\infty = 2.1 \times 10^6$. The pressure coefficient is shown in figure 5. The solution is in reasonable agreement with the experiment. Miller and Wood[25] delineated seven different flow classifications according to leading-edge normal Mach number and angle of attack. The present results, which indicate a primary and secondary vortex with no crossflow shock, are in agreement with Miller's classification.

Since some Reynolds number dependence was found in the previous cases, a wider range of Reynolds numbers were investigated with the thin-layer upwind Navier-Stokes code for laminar flow. Although the grid, Fig. 2, was not refined with increasing Reynolds number, the results are believed to be

generally valid. The pressure coefficient for the various Reynolds numbers is shown in Fig. 6. The leeward suction pressure appears to approach a limit with increasing Reynolds number. The flow fields are similar with the exception of the lowest Reynolds number in which the secondary vortex is not present. Consistent with the experimental results of reference 26, differences with respect to Reynolds number are confined to the size and position of the vortex as well as the peak suction pressure.

Euler Solutions

The Euler solutions (for conical flow) are characterized by the presence of vortical singularities. The entire flow is weakly rotational inside the bow shock due to variable shock strength. Since streamlines terminate at one of the vortical singularities and each streamline crosses the shock at a different location, the flow at the singularities is multivalued. As a practical matter, for the present case, the bow shock is extremely weak and the entropy variation due to the bow shock is negligible.

Inviscid solutions for the central and upwind difference methods are compared on coarse and fine grids. While the two methods agree closely on fine grids, there are dramatic differences on the coarse grid.

Coarse Grid Euler

Since a prime motivation in solving the Euler equations is the desire to avoid the grid fineness necessary for viscous resolution, a coarse grid (75 x 55) was first considered. The minimum step size, $\Delta s/x = 0.005$, gives poor resolution at the tip as can be seen in Fig. 7. The crossflow velocities for the central difference solution are shown in Fig. 8. Corresponding crossflow Mach number and entropy contours are given in Fig. 9. Entropy is defined as

$$\frac{\Delta s}{R} = \frac{s-s_\infty}{R} = \frac{1}{\gamma-1} \ln\left(\left[p/p_\infty\right]/\left[\rho/\rho_\infty\right]^\gamma\right)$$

For constant total enthalpy, total pressure loss is given as

$$\frac{P_o}{P_{o_\infty}} = e^{-\left[\frac{\Delta s}{R}\right]}$$

A comparison of the crossflow velocities, Figs. 4 and 8, reveals a large primary vortex of similar shape and size. Notably absent is the secondary vortex since there is no vorticity generating mechanism on the upper wing surface. A comparison of the pressure coefficient, Fig. 10, for the central difference inviscid and viscous results, shows surprising agreement with the exception of the over expansion at the leading edge. From Fig. 9, it can be seen that entropy is generated at the tip and is convected through the vortex. The entropy and vorticity at the tip are spurious since there is no valid mechanism for their generation in the Euler equations. In the present case, the flow does not separate at the tip but at about 92% of chord on the leeward surface. The separation occurs downstream of a small shock at this point dividing supersonic flows of opposite directions. With less accurate

boundary conditions or large values of the damping coefficient, the point of separation moves closer to the leading edge. In reference 15, several different boundary conditions were tried. The damping coefficient was also varied over its usual range of stability. With minor exceptions in the location of the separation point, the result was always the same - a large primary separation vortex. It should be noted that a minimum value of the damping coefficient was necessary to maintain a stable solution. Computations by E. Murman (Massachusetts Institute of Technology, private communication) for this case, on a similarly coarse grid with a finite volume Runge-Kutta scheme, also resulted in a leading-edge separation vortex.

A better understanding of the separation can be gained by a look at the transient development of the vortex. From the initial condition, the flow quickly expanded about the leading edge to a supersonic crossflow. A crossflow shock also developed on the leeward surface with no separation evident. Concurrently, the leading-edge expansion produced large entropy/vorticity errors which were convected downstream to the developing crossflow shock. The interaction of the two produced a separated region at the base of the shock. The separation then expanded to form the primary vortex and the shock is either absent or confined to the vortex near the tip at the point of separation.

First- and second-order accurate upwind solutions were computed on the same coarse grid. The first-order scheme is the most dissipative scheme considered and does not accurately resolve the detailed flow structure. However, as can be seen in Fig. 11, the flow remains attached at the leading edge. The second-order solution is shown in Fig. 12, and the higher accuracy now correctly predicts the shock-induced vortex centered near the point $y/x = 0.1$. Crossflow Mach number and entropy plots for the second-order accurate solution are given in Fig. 13. The pressure coefficient for the first- and second-order accurate solutions is shown in Fig. 14. As would be expected, the leading-edge expansion and crossflow shock are better resolved with the more accurate differencing. Chakravarthy[27] has also solved the present case with an upwind Euler code on the same coarse grid and found no evidence of leading-edge separation.

Fine Grid Euler

The grid used in the viscous solutions, Fig. 2, was also used for the inviscid calculation. The intent was to reduce the effect of numerically induced errors through better spatial resolution of the tip region. Second-order accurate central and upwind difference solutions are virtually identical on this grid. As can be seen in Fig. 15, the central difference solution is now attached at the leading edge. In both solutions, as in the coarse grid upwind solution, a small vortex appears downstream from the crossflow shock. The vortex is due to shock generated vorticity and is a valid Euler solution. A plot of the crossflow Mach numbers, Fig. 16, shows both the crossflow shock and the shock induced wake. In Fig. 17, enlarged views of the crossflow Mach number and entropy contours are given for the central difference solution. Entropy is generated across the shock according to the local shock strength. It is the entropy variation normal to the streamline which produces the vorticity as required by Crocco's theorem and the subsequent vortex. On the fine grid, the leading-edge expansion is essentially isentropic. This can also be seen in Fig. 18 where the leading-

edge expansion is noticeably sharper than the upwind solution on the coarse grid. The small bump at $y/y_{LE} = 0.3$ is due to the expansion under the vortex.

Since boundary condition error, truncation error, and added artificial dissipation all go to zero in the limit as the grid is refined, it is rather difficult to ascertain the precise cause of the central difference separation. However, when compared with the upwind results, certain possibilities can be eliminated. Both schemes enforce the surface boundary conditions with equivalent accuracy. Since the first-order upwind solution has the largest truncation error and yet remains attached on the coarse grid, the cause of the central difference separation is not just a matter of inadequate numerical resolution. The one distinguishing characteristic between the upwind and central difference methods is the added artificial dissipation model necessary for stability and to control shock oscillations. Although in regions of smooth flow, the added terms are of higher order than the truncation error, in regions of large gradients, the pressure switch built into the model causes the scheme to revert to first order. For this reason, it has been widely speculated, but not proven, that the artificial dissipation model is responsible for spurious inviscid separation. It is interesting to note, in comparing entropy generation at the tip between the central and upwind solutions on the coarse grid (Figs. 9 and 13), that although the upwind value is lower (0.3) than the central difference value (0.6), the terms are of the same order of magnitude.

SHARP LEADING EDGES

Navier-Stokes Solutions

A thin-layer Navier-Stokes solution was computed for the thin, sharp-edged wing at a Reynolds number, $Re_\infty = 0.1 \times 10^6$, using the second-order accurate scheme. The grid, Fig. 19, consisted of 151 x 65 points with a minimum step size $\Delta s/x = 0.0002$. The crossflow velocities, Fig. 20, exhibit the same primary and secondary vortices at the same locations as the rounded leading edge. Crossflow Mach contours are given in Fig. 21.

Euler Solutions

Since the upwind code was found to be much less susceptible to spurious inviscid separation for rounded leading edges, its behavior for sharp leading edges was investigated. The essential difference is that, unlike the rounded leading edge, the local behavior at the sharp edge is singular. Both first- and second-order solutions were computed on coarse and fine grids. Because of the very large gradients in the flow near the tip, it was found necessary to use first-order interpolation (equation 13) in the flux calculations for some 3-4 points away from and on either side of the tip in the second-order solutions. This type of flux limiting has been used (ref. 28) to ensure monotone shock profiles for strong shocks. The calculation remains fully conservative.

Coarse Grid Euler

The coarse grid, Fig. 22, consisted of 75 x 55 points. The local tip resolution is significantly less than that of the sharp tip viscous grid, Fig. 19. On this grid, both first- and second-order solutions are attached at the

leading edge. The second-order solution predicts a vortex downstream of the crossflow shock as can be seen in Fig. 23. Crossflow Mach number and entropy contours for the second-order solution are given in Fig. 24. Despite the presence of large entropy errors generated at the tip, leading-edge separation does not occur. The pressure coefficient, Fig. 25, is similar to the rounded edge result with a well-defined crossflow shock.

Zero-Thickness Wing

A zero thickness wing was considered in order to determine if attached flow solutions could be obtained in this extreme case. Powell et al.[12] recently presented leading-edge vortex solutions for similar geometries using a finite volume central difference scheme. The grid dimensions were the usual 151 x 65 points. However, as seen in Fig. 26, the local resolution at the tip is relatively coarse. The first-order solution did not exhibit leading-edge separation. The crossflow velocities, Fig. 27, show a vortex downstream of the crossflow shock. Crossflow Mach number and entropy are given in Fig. 28. The second-order solution exhibits leading-edge separation, as is evident in Fig. 29. Both solutions are first-order accurate at the leading edge. Although the (pseudo) transient development of the two solutions was not observed, it is presumed that the interaction of the crossflow shock with the rotationality induced at the leading edge is unstable in the more accurate calculation. As a consequence, the flow separates at the base of the crossflow shock and the separation bubble grows to form the primary vortex. In Fig. 30, it can be seen that the crossflow shock has been displaced to a position above the vortex near its inboard boundary. The pressure coefficient for the two solutions is given in Fig. 31. The second-order solution has been compared with the results obtained by K. Powell and E. Murman (Massachusetts Institute of Technology, private communication). Although the comparison is not shown, the two computations are in close agreement, including the level of minimum pressure coefficient and the extent and shape of the separation vortex.

Fine Grid Euler

Upwind Euler solutions were computed for the thin, sharp-tipped wing using the finer viscous grid, Fig. 19. In contrast to the previous coarse grid calculations, both the first- and second-order solutions are separated at the leading edge. The first-order solution predicts a very shallow vortex extending from the leading edge to the centerline. The second-order solution predicts the more familiar separation vortex. The crossflow velocity plot, Fig. 32, reveals two smaller secondary vortices near the leading edge. Referencing the crossflow Mach number plot, Fig. 33, the secondary vortices are triggered by a small crossflow shock embedded in the vortex. These features were not found in the viscous calculation, $Re_\infty = 0.1 \times 10^6$, Fig. 20. The inviscid calculation also predicts a crossflow shock above the vortex near the inboard boundary which is not present in the viscous result. A thin layer (laminar) viscous calculation at a Reynolds number of $Re_\infty = 50 \times 10^6$ also failed to exhibit the inviscid shock-induced secondary vortices. The pressure coefficient at the lower Reynolds number is compared with the viscous solution in Fig. 34.

CONCLUSIONS

Central and upwind difference solutions to the Euler and Navier-Stokes equations have been presented for conical delta wings with several cross-sectional shapes. For the rounded leading edge, central and upwind difference Navier-Stokes solutions agree well. Although adequate resolution is necessary for accurate results, the Navier-Stokes equations describe all relevant physical mechanisms and provide a consistent flow description. On a coarse grid, the central difference Euler solution predicts a primary separation vortex which resembles the viscous result. This separation vortex, however, is due entirely to numerical error. With sufficient grid refinement, the vortex disappears. On both coarse and fine grids, the upwind solution does not produce leading-edge separation. Both methods correctly predict shock-induced inviscid separation on the fine grid. The separation in this case is a valid Euler solution. Upwind solutions to the Navier-Stokes and Euler equations were computed for sharp leading-edge geometries. The viscous solutions again represent a consistent physical model. Attached flow Euler solutions were found for very sharp leading edges and even for the infinitely thin zero thickness wing. However, with sufficient grid refinement or resort to higher order spatial accuracy, the upwind scheme also predicts leading-edge separation.

The behavior of central and upwind difference schemes in the solution of the Euler equations for flow about the leading edges of highly swept delta wings raises questions of theoretical and practical importance. In this paper, the emphasis has been on the latter question. As a model for the prediction of leading-edge separation vortices, the Euler equations lack the essential quality of consistency. Further, they are fundamentally incapable of predicting secondary flow features such as Reynolds numbers dependence or the presence of secondary vortices. On the same grid, the cost of evaluating the viscous terms in the thin layer Navier-Stokes equations relative to the inviscid Euler equations is less than a 2% increase in CPU time per iteration for the implicit upwind code. This figure reflects the fact that a majority of the CPU time is spent assembling and solving the linear systems arising from the the implicit time discretization. The penalty for an explicit method is significantly higher. In any event, the increase in accuracy and consistency in the resulting solutions would seem to justify the marginal increase in computational cost.

REFERENCES

1. Vigneron, Y. C.; Rakich, J. V.; and Tannehill, J. C.: Calculation of Supersonic Viscous Flow Over Delta Wings With Sharp Subsonic Leading Edges. AIAA Paper 78-1137, July 1978.

2. Fujii, K.; and Kutler, P.: Numerical Simulation of the Leading Edge Separation Vortex for a Wing and Strake-Wing Configuration. AIAA Paper 83-1908, July 1983.

3. Fujii, K.; and Kutler, P.: Numerical Simulation of the Viscous Flow Over Three-Dimensional Complicated Geometries. AIAA Paper 84-1550, June 1984.

4. Rizzetta, D. P.; and Shang, J. S.: Numerical Simulation of Leading Edge Vortex Flows. AIAA Paper 84-1544, June 1984.

5. Hitzel, S. M.; and Schmidt, W.: Slender Wings With Leading-Edge Vortex Separation - A Challenge for Panel-Methods and Euler Codes. AIAA Paper 83-0562, Jan. 1983.

6. Rizzi, A.: Damped Euler-Equation Method to Compute Transonic Flow Around Wing-Body Combinations. AIAA Journal, vol. 20, no. 10, Oct. 1982, pp. 1321-1328.

7. Rizzi, A.; Eriksson, L. E.; Schmidt, W.; and Hitzel, S. M.: Simulating Vortex Flows Around Wings. Aerodynamics of Vortical Type Flows in Three Dimensions, AGARD Conference Preprint No. 342, 1983.

8. Rizzi, A.; and Erickson, L. E.: Computation of Flow Around Wings Based on the Euler Equations. Journal of Computational Physics, vol. 148, 1984, pp. 45-71.

9. Rizzi, A.: Euler Solutions of Transonic Vortex Flow Around the Dillner Wing - Compared and Analyzed. AIAA Paper 84-2142, Aug. 1984.

10. Rizzi, A.: Modelling Vortex Flow Fields by Supercomputers With Supersize Memory. Aeronautical Journal, April 1985, pp. 149-161.

11. Raj, P.; and Sikora, J.: Free Vortex Flows: Recent Encounters With an Euler Code. AIAA Paper 84-0135, Jan. 1984.

12. Powell, K.; Murman, E.; Perez, E.; and Baron, T.: Total Pressure Loss in Vortical Solutions of the Conical Euler Equations. AIAA Paper 85-1701, July 1985.

13. Fujii, K.; and Obayashi, S.: Evaluation of Euler and Navier-Stokes Solutions for Leading-Edge and Shock-Induced Separations. AIAA Paper 85-1563, July 1985.

14. Manie, F.; Neron, M.; and Schmitt, V.: Experimental and Computational Investigation of the Vortex Flow Over a Swept Wing. 14th Congress of the International Council of the Aeronautical Sciences, ICAS-84-2.8.1, Sept. 1984.

15. Newsome, R.: A Comparison of Euler and Navier-Stokes Equations for Supersonic Flow Over a Conical Delta Wing. AIAA Paper 85-0111, Jan. 1985.

16. Salas, M. D.: Recent Developments in Transonic Euler Flow Over a Circular Cylinder. Mathematics and Computers in Simulation, vol. 25, 1983, pp. 232-236.

17. Marconi, F.: The Spiral Singularity in the Supersonic Inviscid Flow Over a Cone. AIAA Paper 84-0135, Jan. 1984.

18. Marconi, F.: Shock Induced Vorticities on Elliptic Cones in Supersonic Flow. AIAA Paper 85-0433, Jan. 1985.

19. Salas, M. D.; and Daywitt, J.: Structure of the Conical Flow Field About External Axial Corners. AIAA Journal, vol. 17, no. 1, pp. 41-47, Jan. 1979.

20. Thomas, J. L.; van Leer, B.; and Walters, R. W.: Implicit Flux-Split Schemes for the Euler Equations. AIAA Paper 85-1680, July 1985.

21. Thomas, J. L.; and Walters, R. W.: Upwind Relaxation Algorithms for the Navier-Stokes Equations. AIAA Paper 85-1501 CP, July 1985.

22. MacCormack, R. W.: Numerical Solutions of the Interactions of a Shock Wave With a Laminar Boundary Layer. Lecture Notes in Physics, vol. 59, Springer Verlag, 1970, pp. 151-163.

23. MacCormack, R. W.; and Baldwin, B. S.: A Numerical Method for Solving the Navier-Stokes Equations With Application to Shock-Boundary Layer Interactions. AIAA Paper 75-1, Jan. 1975.

24. Squire, L. C.: Leading-Edge Separation and Crossflow Shocks on Delta Wings. AIAA Journal, vol. 23, no. 9, March 1985, pp. 321-325.

25. Miller, D. S.; and Wood, R. M.: An Investigation of Wing Leading-Edge Vortices at Supersonic Speeds. AIAA Paper 83-1816, July 1983.

26. Szodruch, J.: Reynolds Number Influence on Leeside Flow Fields, AIAA Journal, vol 16., no. 12, Dec. 1978, pp. 1306-1309.

27. Chakravarthy, S.; and Ota, D.: Numerical Issues in Computing Invicid Supersonic Flow Over Conical Delta Wings. AIAA Paper 86-0440, January 1986.

28. Walters, R. W.; and Dwoyer, D. L.: An Efficient Strategy Based on Upwind/Relaxation Schemes for the Euler Equations. AIAA Paper 85-1529-CP, July 1985.

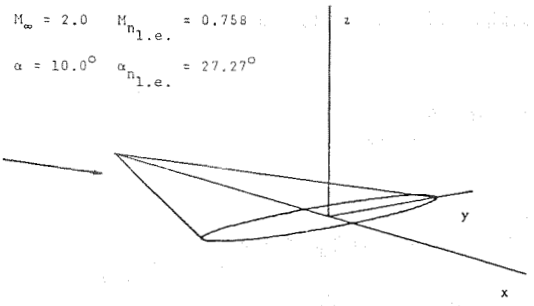

Fig. 1 Elliptic cone, $y_{LE}/x = \tan(20°)$, $z_{CL}/x = \tan(1.5°)$.

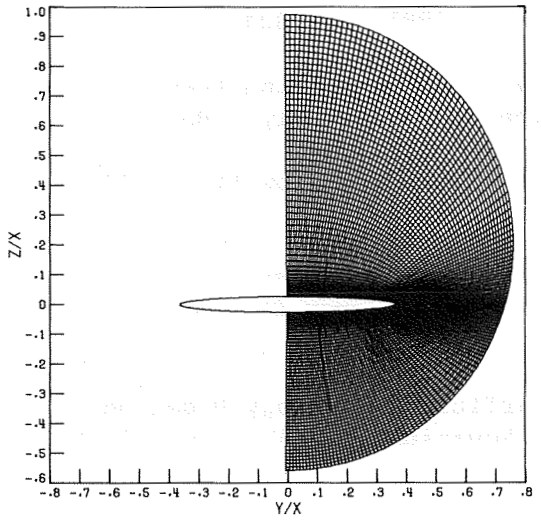

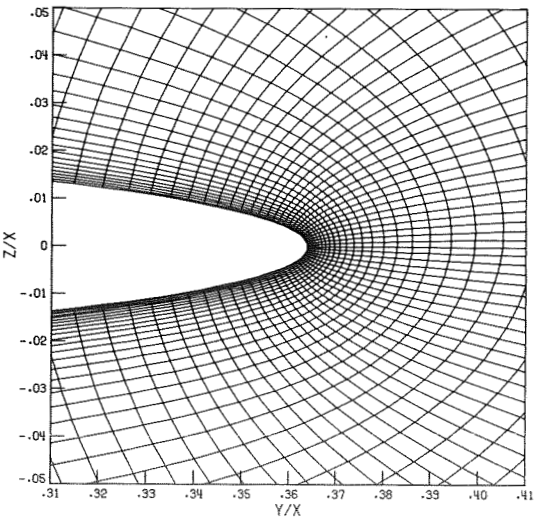

Fig. 2 Fine grid (151 × 65 points).

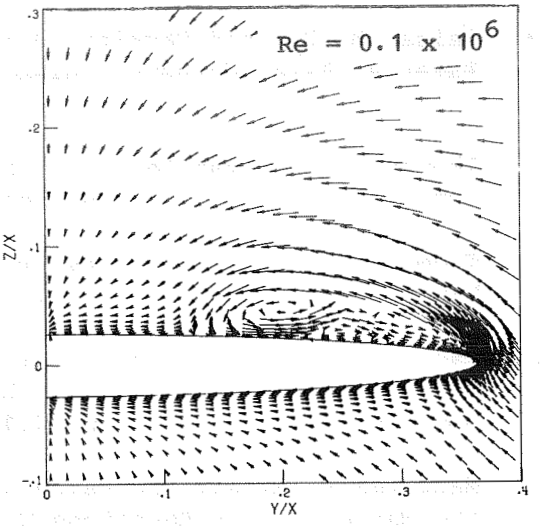

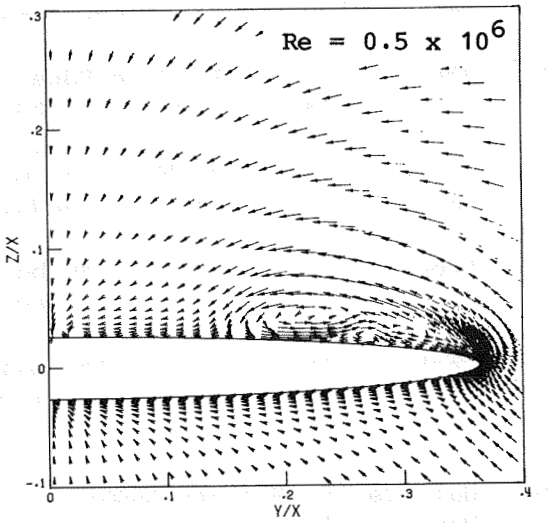

Fig. 3 Crossflow velocity vectors, central difference Navier-Stokes.

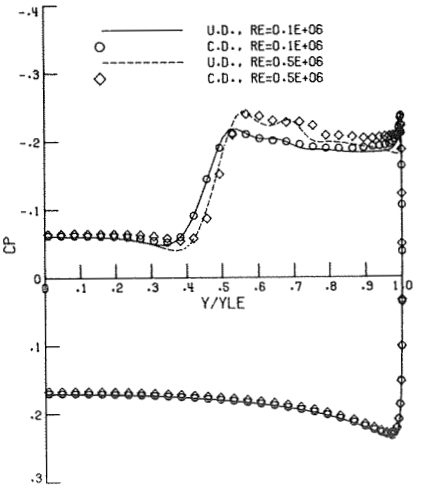

Fig. 4 Pressure coefficient, central and upwind difference Navier-Stokes.

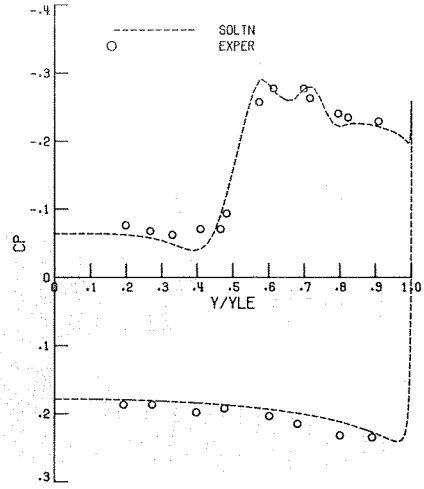

Fig. 5 Pressure coefficient, upwind difference Navier-Stokes versus data of Squire.

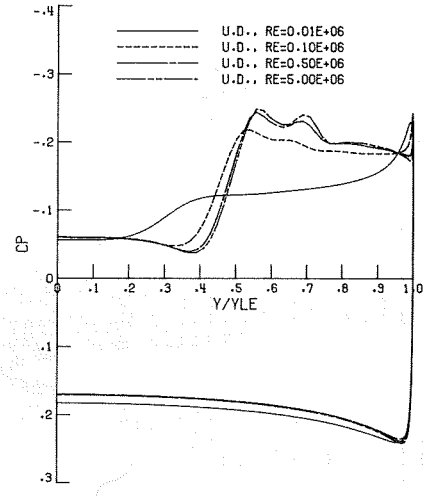

Fig. 6 Pressure coefficient, sensitivity to Reynolds number, upwind difference Navier-Stokes.

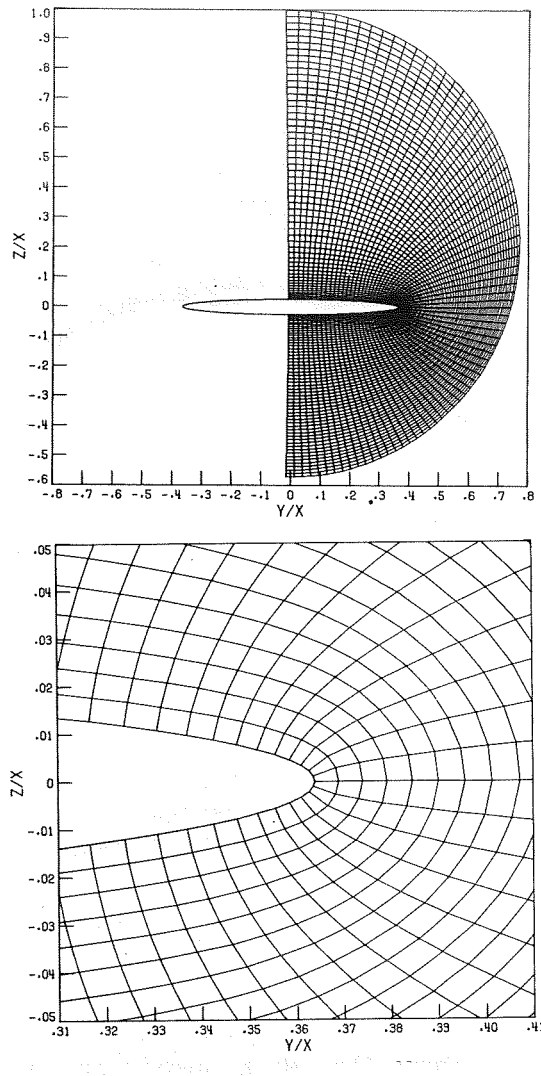

Fig. 7 Coarse grid (75 × 55 points).

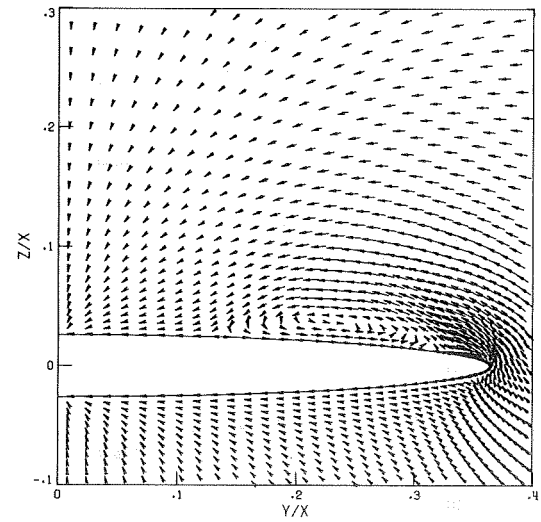

Fig. 8 Crossflow velocity vectors, central difference Euler, coarse grid.

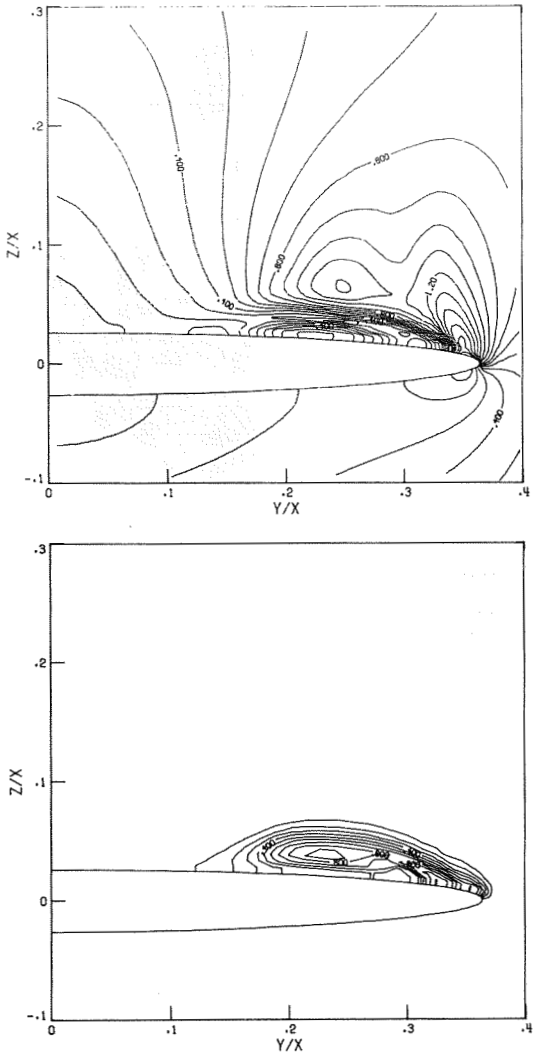

Fig. 9 Crossflow Mach number and entropy contours, coarse grid, central difference Euler.

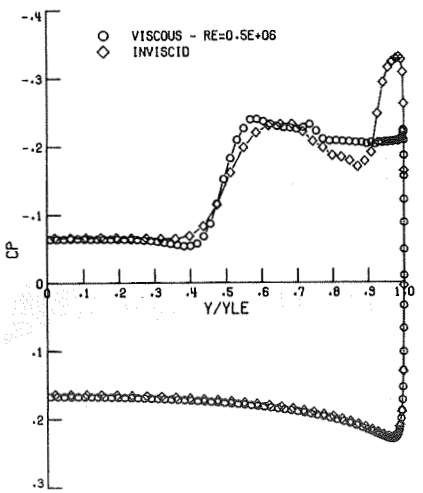

Fig. 10 Pressure coefficient, central difference coarse grid Euler versus fine grid Navier-Stokes.

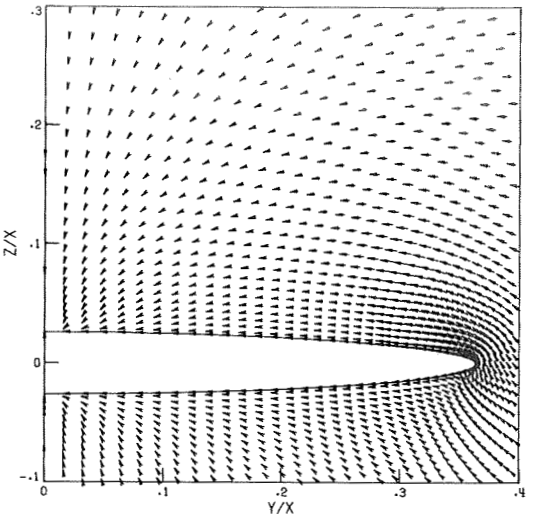

Fig. 11 Crossflow velocity vectors, coarse grid, 1st-order, upwind Euler.

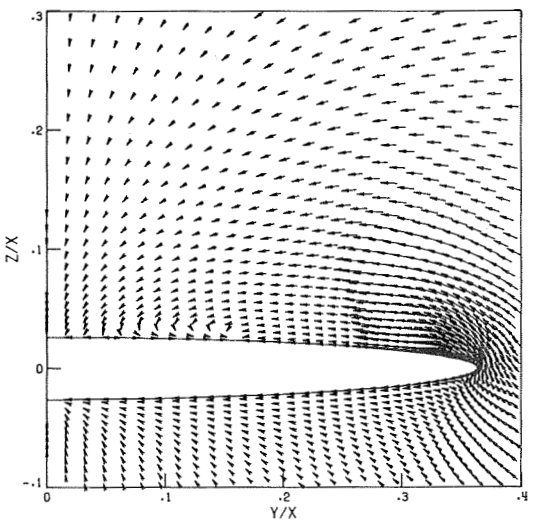

Fig. 12 Crossflow velocity vectors, coarse grid, 2nd-order upwind Euler.

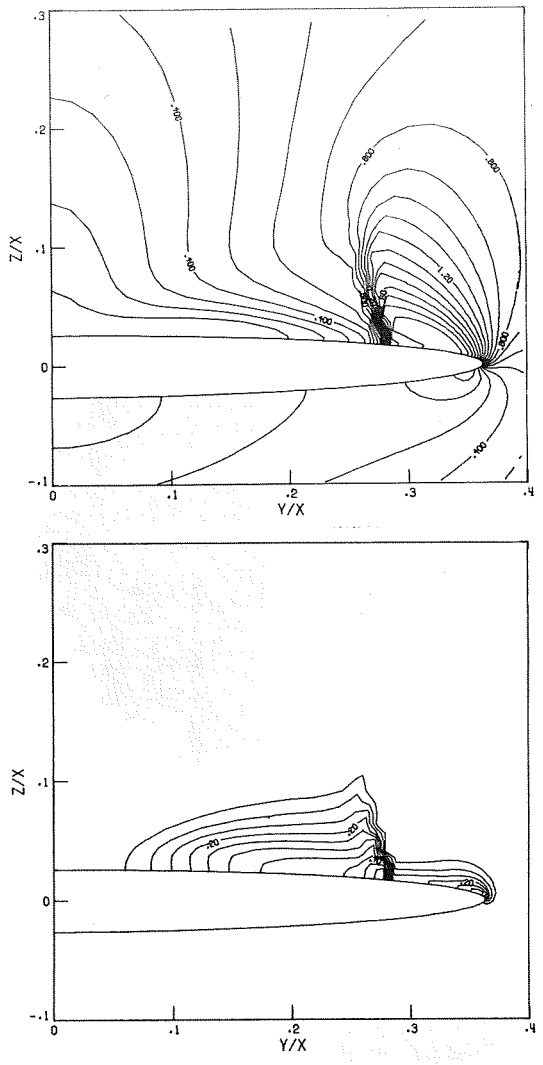

Fig. 13 Crossflow Mach number and entropy contours, coarse grid 2nd-order upwind Euler.

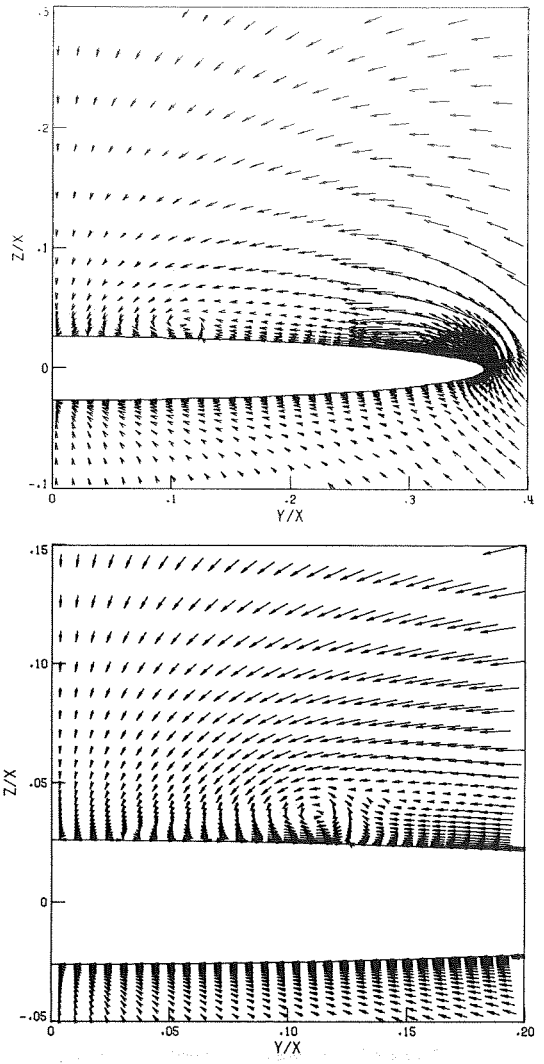

Fig. 15 Crossflow velocity vectors, fine grid central difference Euler.

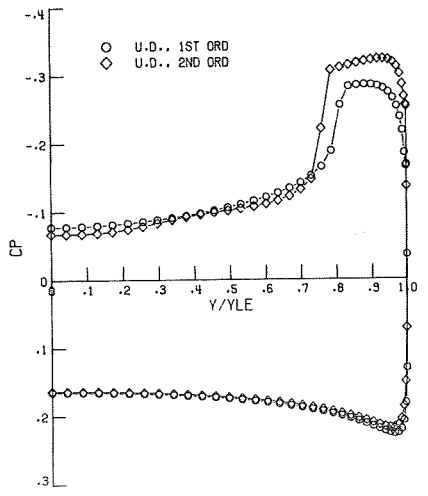

Fig. 14 Pressure coefficient, coarse grid 1st- and 2nd-order upwind Euler.

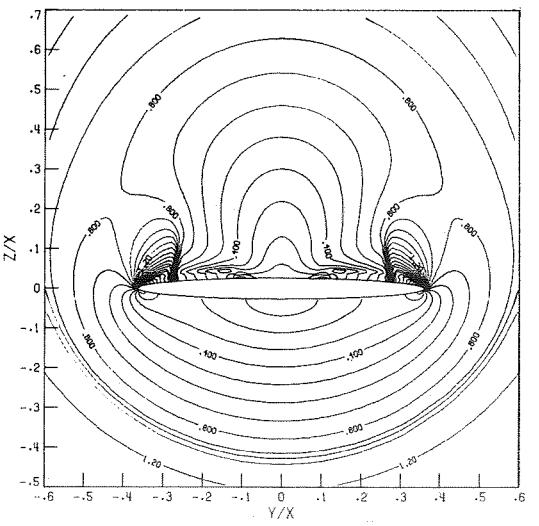

Fig. 16 Crossflow Mach number, fine grid, central difference Euler.

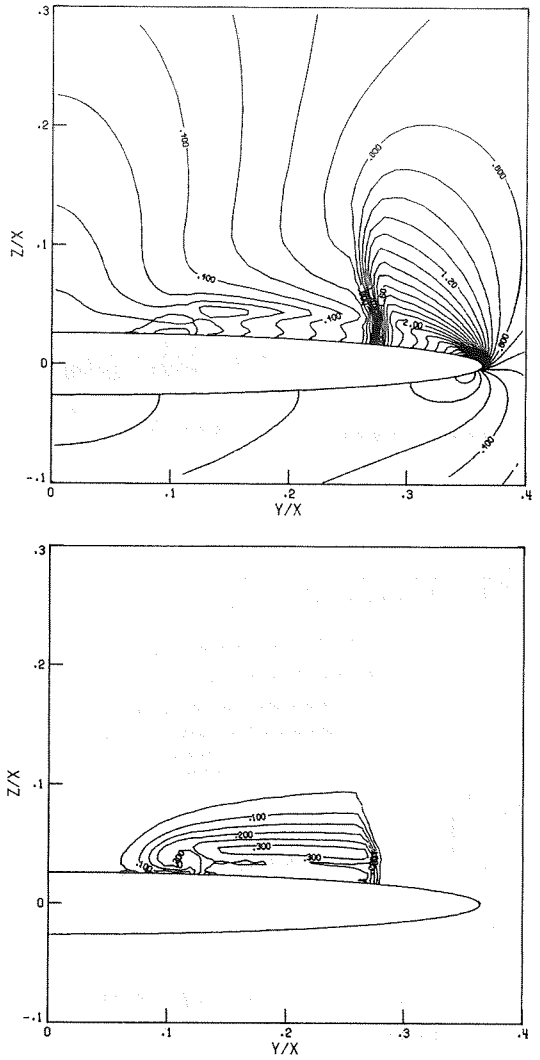

Fig. 17 Crossflow Mach number and entropy contours, fine grid central difference Euler.

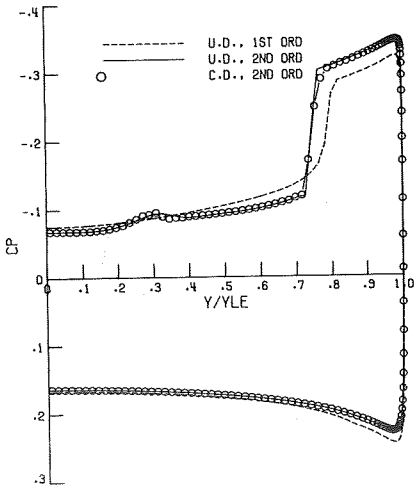

Fig. 18 Pressure coefficient, fine grid, central difference Euler versus upwind difference Euler.

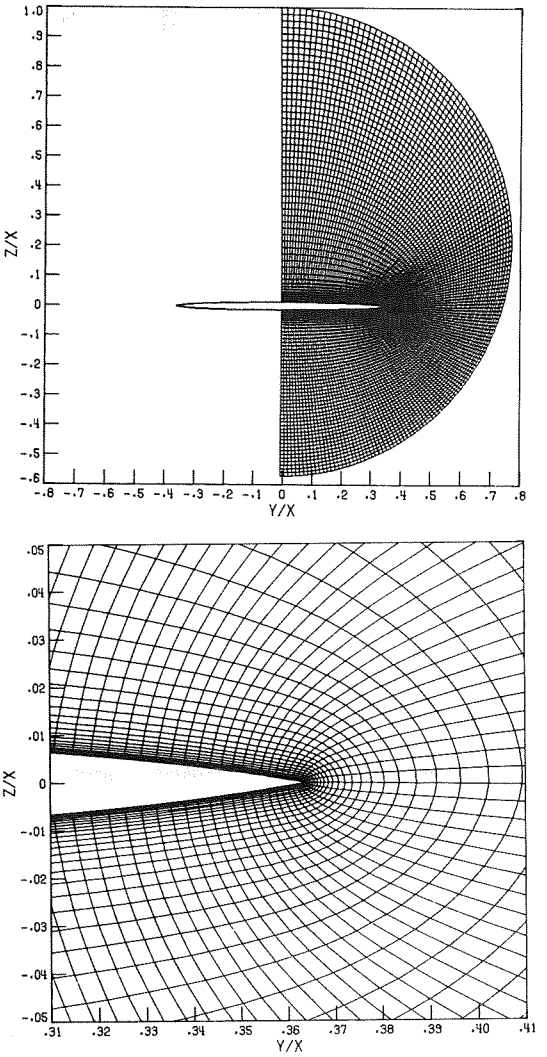

Fig. 19 Fine, sharp tip, grid (151 × 65) points.

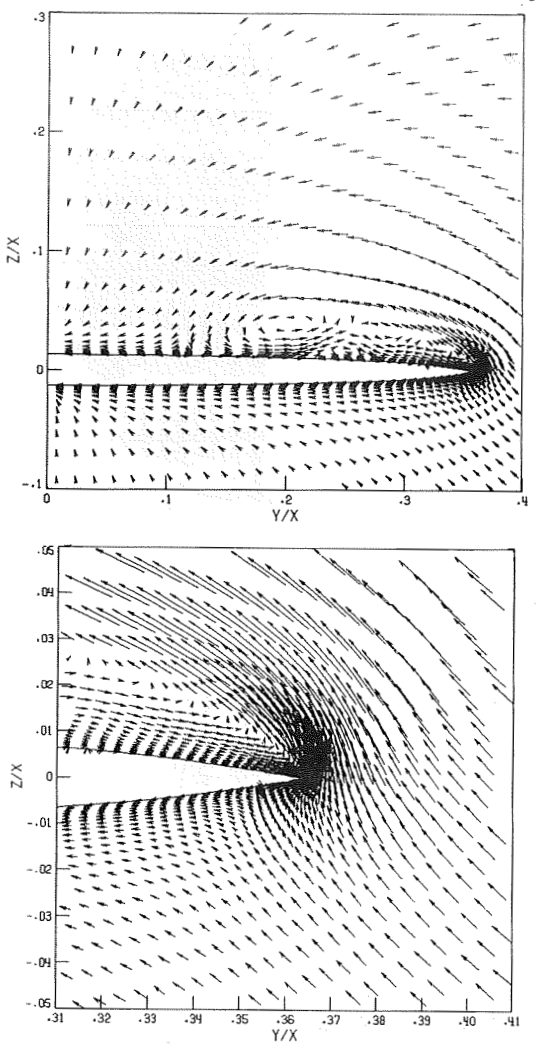

Fig. 20 Crossflow velocity vectors, fine grid, upwind differnce Navier-Stokes, Re = 0.1×10^6.

Fig. 21 Crossflow Mach number, fine grid, upwind difference Navier-Stokes, Re = 0.1×10^6.

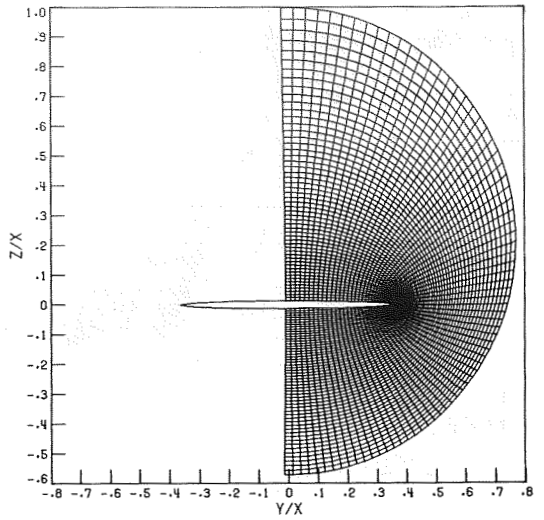

Fig. 22 Coarse, sharp tip, grid (75 × 55 points).

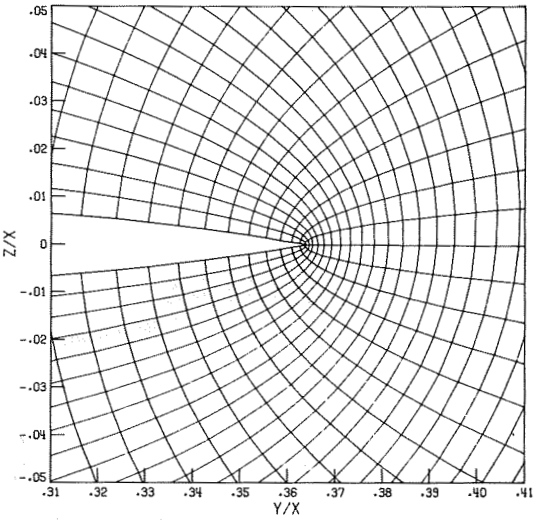

Fig. 23 Crossflow velocity vectors, coarse grid 2nd-order, upwind Euler.

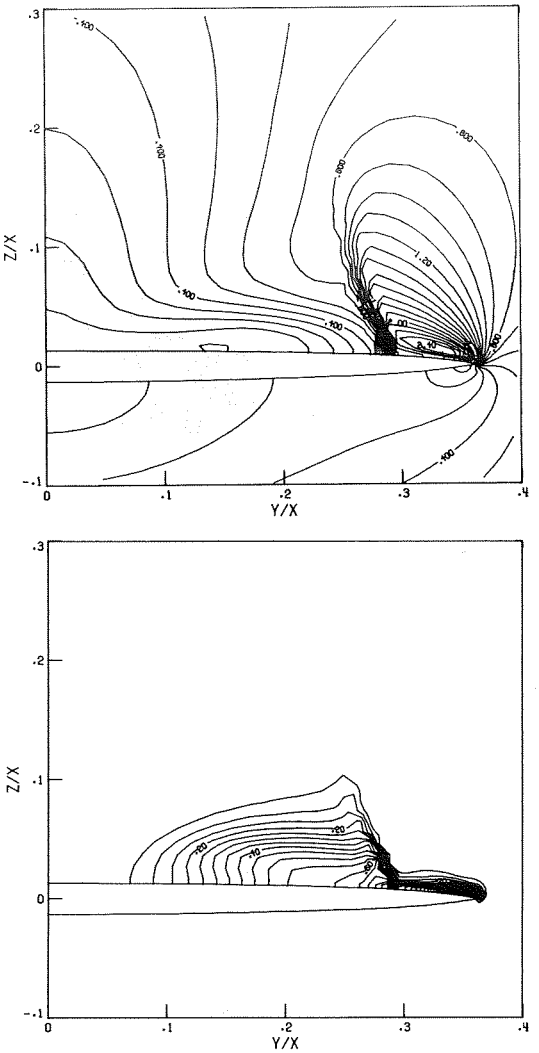

Fig. 24 Crossflow Mach number and entropy contours, coarse grid, 2nd-order, upwind Euler.

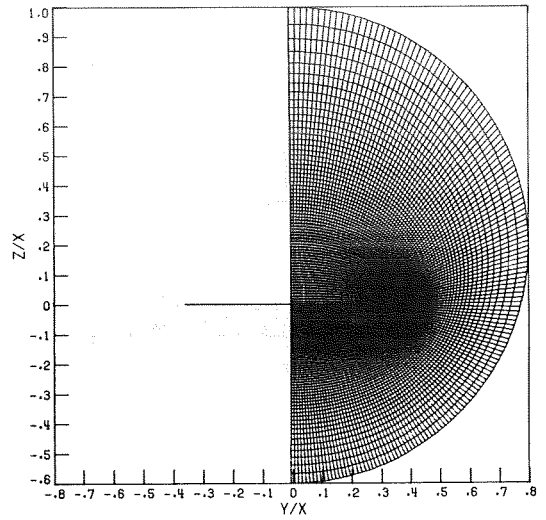

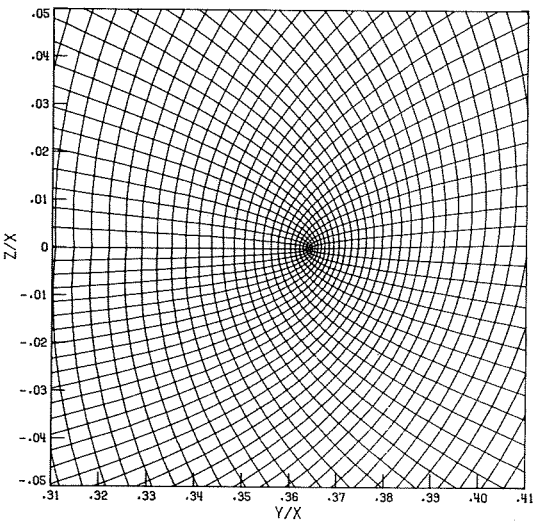

Fig. 26 Zero thickness wing grid (151 × 65 points).

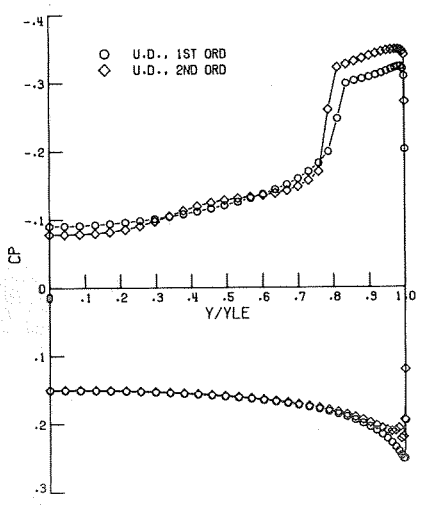

Fig. 25 Pressure coefficient, coarse grid 1st- and 2nd-order upwind Euler.

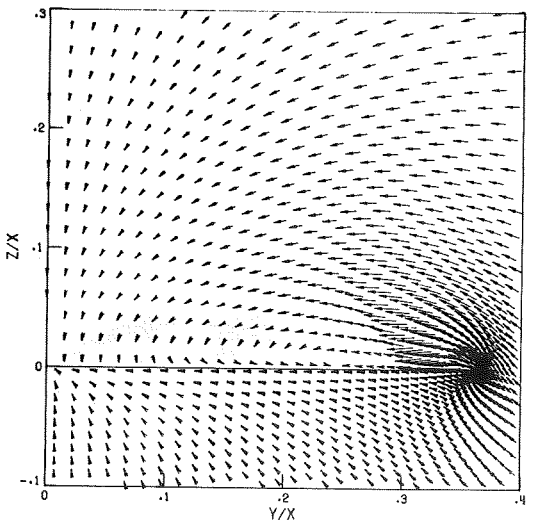

Fig. 27 Crossflow velocity vectors, zero thickness wing, 1st-order upwind Euler.

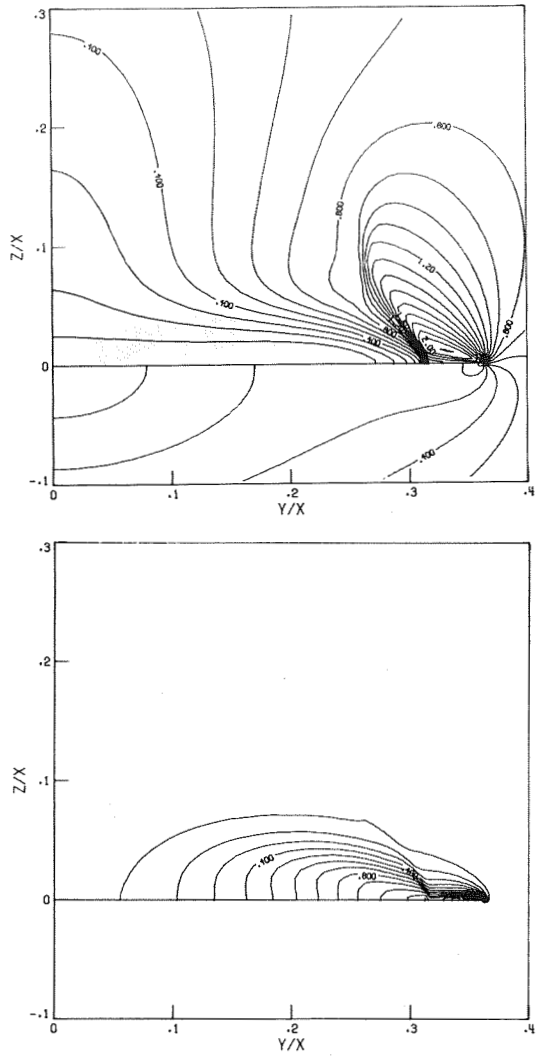

Fig. 28 Crossflow Mach number and entropy contours, zero thickness wing, 1st-order upwind Euler.

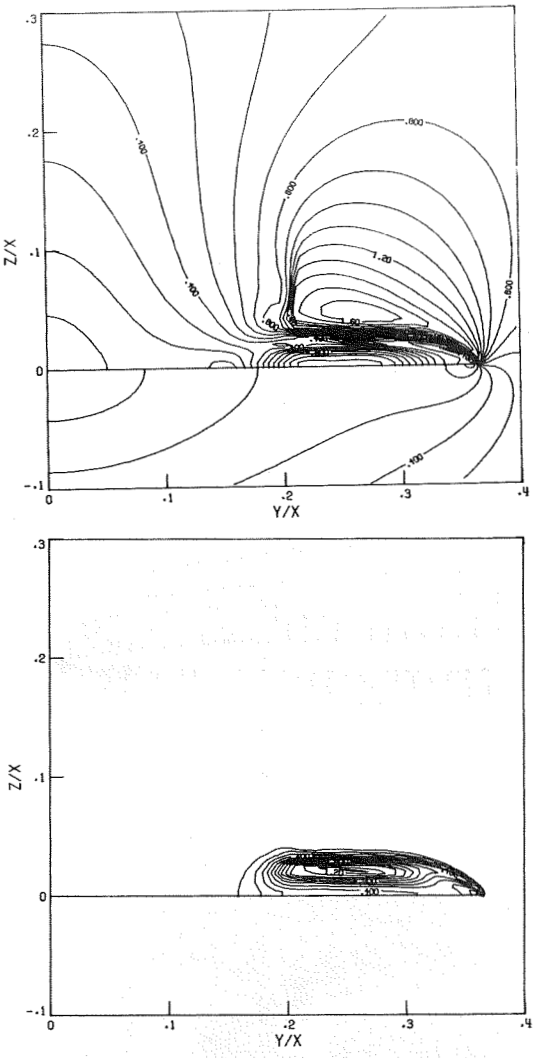

Fig. 30 Crossflow Mach number and entropy contours, zero thickness wing 2nd-order upwind Euler.

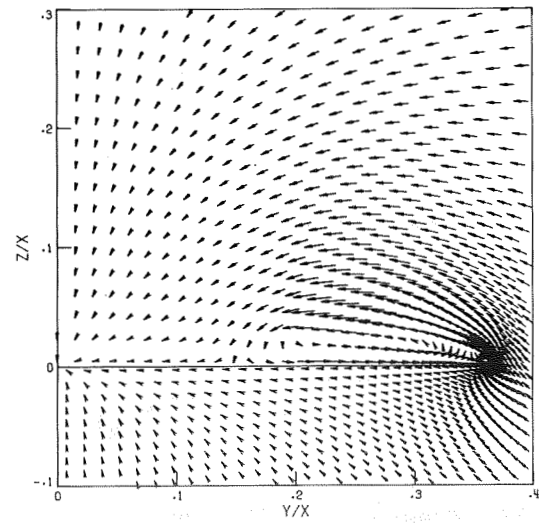

Fig. 29 Crossflow velocity vectors, zero thickness wing, 2nd-order upwind Euler.

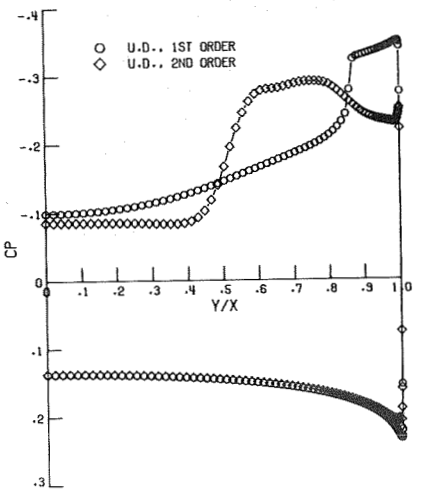

Fig. 31 Pressure coefficient, zero thickness wing, 1st- and 2nd-order upwind Euler.

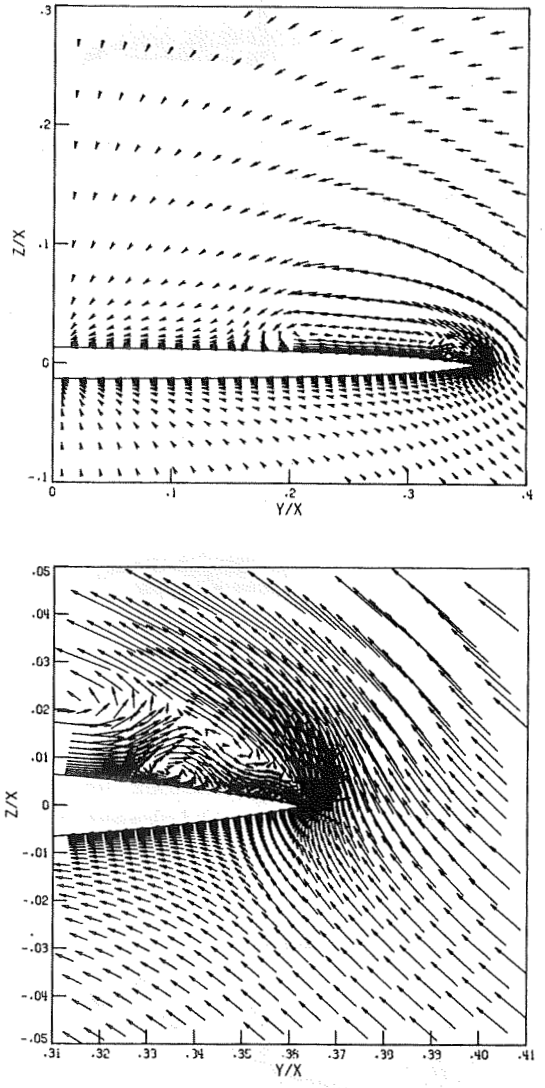

Fig. 32 Crossflow velocity vectors, fine grid, 2nd-order, upwind Euler.

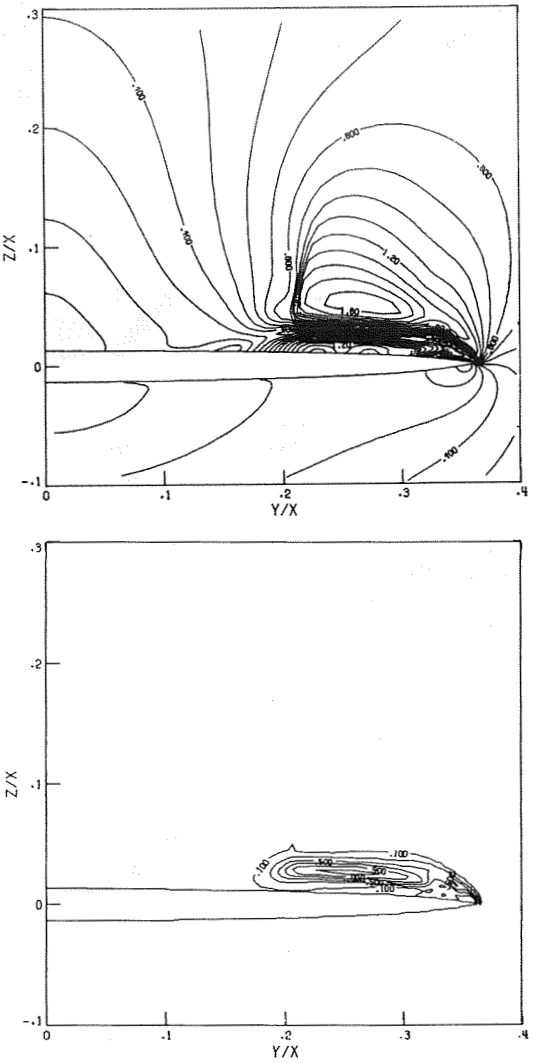

Fig. 33 Crossflow Mach number and entropy contours, fine grid, 2nd-order upwind Euler.

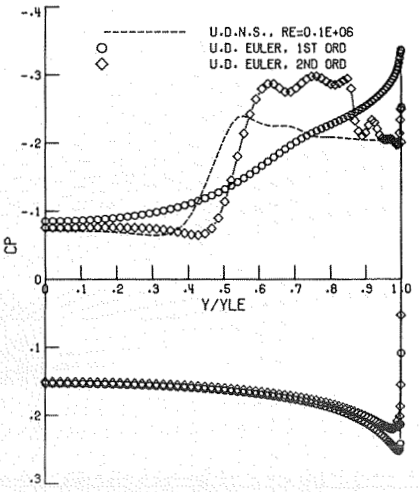

Fig. 34 Pressure coefficient, fine grid, 1st- and 2nd-order upwind Euler versus upwind Navier-Stokes Re = 0.1×10^6.